Orientation Space Filtering for Multiple Orientation Line Segmentation

Jian Chen, *Member*, *IEEE*, Yoshinobu Sato, *Member*, *IEEE*, and Shinichi Tamura, *Member*, *IEEE*

Abstract—The goal of this paper is to present an appropriate method for the segmentation of lines at intersections (X-junctions) and branches (T-junctions), which can be regarded as local regions where lines occur at multiple orientations. A novel representation called "orientation space" is proposed, which is derived by adding the orientation axis to the abscissa and the ordinate of the image. The orientation space representation is constructed by treating the orientation parameter, to which Gabor filters can be tuned, as a continuous variable. The problem of segmenting lines at multiple orientations is dealt with by thresholding 3D images in the orientation space and then detecting the connected components therein. In this way, X-junctions and T-junctions can be separated effectively. Curve grouping can also be accomplished. The segmentation of mathematically modeled X-, T-, and L-junctions is demonstrated and analyzed. The sensitivity limits of the method are also discussed. Experimental results using both synthesized and real images show the method to be effective for junction segmentation and curve grouping.

Index Terms—Line segmentation, multiple orientation lines, junctions, orientation bandwidth, orientation space.

1 Introduction

Line segmentation is widely used to extract curvilinear structures as diverse as blood vessels in medical image analysis [1], strokes in character recognition [2], [3], motion and structure from multiple images [4], [5], and roads in satellite image analysis [6], [7]. Since width and orientation are the predominant and most informative features that characterize a line, it is appropriate to analyze these two parameters to segment lines in early vision. To detect and separate intersections and branches, it is necessary to analyze lines at local regions such as X- and T-junctions where lines exist at multiple orientations. Koller et al. [8] employed a nonlinear combination of linear multiple scale filters to detect lines of various widths and select only a single orientation for each pixel, but multiple orientations were not considered in their method. Steger [9] recently proposed an explicit model for lines and their surroundings to extract lines and line widths with high precision; however, this method cannot deal with junction segmentation because the direction of a line is estimated by an eigenvector corresponding to the maximal absolute value of the Hessian matrix eigenvalue. The key issues in segmenting lines at multiple orientations are:

1. how to represent multiple orientations at local regions, i.e., junctions and
2. how to robustly extract the multiple orientation features.

- *J. Chen is with the Department of Radiology, Weill Medical College of Cornell University, 515 East 71st Street, S-Building, New York, NY 10021. E-mail: jic2003@med.cornell.edu.*
- *Y. Sato and S. Tamura are with the Division of Functional Diagnostic Imaging, Biomedical Research Center, Osaka University Graduate School of Medicine, 2-2 Yamadaoka, Suita, Osaka 565-0871, Japan. E-mail: {yoshi, tamuras}@image.med.osaka-u.ac.jp.*

Manuscript received 8 June 1998; accepted 9 Feb. 2000.
Recommended for acceptance by R. Chellappa.
For information on obtaining reprints of this article, please send e-mail to: tpami@computer.org, and reference IEEECS Log Number 107825.

In this paper, which has already appeared in a preliminary form in [10], we first focus on line orientation, and then on multiple orientation line segmentation. Work on the segmentation of lines at multiple orientations can be divided into two categories: orientation and junction analysis, and curve grouping and segmentation.

There are a considerable number of studies in the literature relating to orientation and junction analysis [11] [12], [13], [14], [15], [16], [17], [18], 19]. Perona proposed detecting junction edges by searching for local maximal responses with respect to continuous orientation [14], [18], [19]. Here, we employ the concept of continuous orientation set out by Perona and extend it to formulate a simple yet powerful method for segmenting lines at multiple orientations. We construct a representation in the form of a three-dimensional "orientation space," which is derived by adding the orientation axis to the abscissa and the ordinate of the image, and then formulate the problem of multiple orientation segmentation as one of analyzing the 3D images of the orientation space.

Curve grouping and segmentation received a large amount of attention in early vision [20], [21], [22], [23], [24], [25]. A smooth curve can be parameterized by the length of an arc extending from a fixed point thereon to another point. The winding angle, which is defined as the cumulative angle described by the tangent as the curve advances from the start point, varies continuously along the arc length. Hence, multiple orientations exist at local regions where curve intersections occur, as well as along each curve. Consequently, we contend that the problem of curve grouping can be regarded as one of multiple orientation line segmentation. We utilize the winding angle as a controlled orientation parameter and then deal with curve grouping and segmentation in orientation space.

The orientation space representation is constructed by treating the orientation parameter, to which Gabor filters can be tuned, as a continuous variable. In this way, the

real component of a complex Gabor filter, which is characterized by an even symmetric receptive-field function, can be employed to enhance the lines in an image. The segmentation of lines at multiple orientations is achieved by thresholding 3D images in the orientation space and then detecting the connected components therein. The connected components group the orientation continuities of lines and dissolve the global discontinuities caused by intersecting lines or curves in the orientation space. In constructing the orientation space, the selection of a suitable orientation bandwidth for the Gabor filters is important. If the orientation bandwidth is small, the orientation selectivity is high, while the filter response of a line having a high degree of curvature is low, that is, the sensitivity to the line is low. We therefore need to achieve a good trade-off of sensitivity and selectivity for optimum multiple orientation line segmentation.

The paper is organized as follows: Section 2 describes the method used to construct the orientation space using Gabor filters as tunable filters to represent lines at multiple orientations. In Section 3, the concept of multiple orientation line segmentation using the orientation space is formulated. In Section 4, we address the sensitivity limits of the proposed method for segmentation of X-, T-, and L-junctions, analytically given by mathematical line models, and reveal the influences of selecting the filter scale on the sensitivity to junction segmentation. In Section 5, experimental results using synthesized image, biomedical images, and a scanned Japan character image are presented. Finally, in Section 6, we compare our work with previous related studies and summarize our conclusions.

2 Orientation Space Representation Based on Gabor Filter

To extract lines that have an even symmetric structure, we use as our tunable filter the real component of a complex Gabor filter [26], which is characterized by an even symmetric receptive-field function. The filter, which is tuned to an arbitrary orientation to represent lines at multiple orientations, is given by

$$f^{\theta}(x,y;\sigma,\lambda,\omega)=\frac{1}{2\pi\sigma^2\lambda}\exp\left\{-\frac{\lambda^2x'^2+y'^2}{2\lambda^2\sigma^2}\right\}\cos(2\pi\omega x'), \quad (1)$$

where $(x',y')=(x\cos\theta+y\sin\theta,-x\sin\theta+y\cos\theta)$, θ is the preferred orientation parameter by which the filter is tuned, ω is the radial center frequency, and λ is the aspect ratio of the standard deviation along y to σ—which is the standard deviation along x. In the frequency domain, the filter is represented by

$$F^{\theta}(U,V;\sigma,\lambda,\omega)= \frac{1}{2}\left\{\exp[-2\pi^2\sigma^2(U'+\omega)^2]+\exp[-2\pi^2\sigma^2(U'-\omega)^2]\right\} \exp(-2\pi^2\sigma^2\lambda^2V'^2), \quad (2)$$

where $(U',V')=(U\cos\theta+V\sin\theta,-U\sin\theta+V\cos\theta)$.

Fig. 1 depicts a half-peak of the Gabor filter in the frequency domain. The orientation bandwidth Ω of the filter is given by

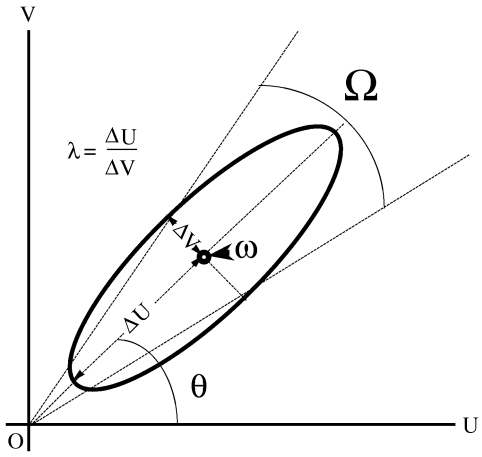

Fig. 1. Contour giving a half-peak of the Gabor filter in the frequency domain, with aspect ratio λ, radial center frequency ω, and orientation θ. Ω denotes the orientation bandwidth of the Gabor filter, and $\triangle U$ and $\triangle V$ represent the effective widths with respect to U and V. Here, $\triangle U\approx\frac{1}{2\pi\sigma}$ and $\triangle V\approx\frac{1}{2\pi\sigma\lambda}$.

$$\Omega\approx 2\arctan\left(\frac{1}{2\pi\sigma\omega\lambda}\right). \quad (3)$$

As shown in (3), the orientation bandwidth varies inversely as the product of $\sigma\omega\lambda$. When the orientation bandwidth is small, the orientation selectivity of the filter is high.

Lines can exist at all possible orientations and multiple orientations will occur at local regions such as line intersections. In order to represent such multiple orientations at each pixel, an orientation space is constructed by treating the orientation parameter θ to which the filter is tuned as a continuous variable. Based on the orientation bandwidth, the orientation space representation of an image is an embedding of the image into the orientation parameter θ family of derived images constructed by convolution with the orientation parameter θ family of the kernels of the tunable filter. Let $I(x,y)$ represent any given image. Based on the filter $f^{\theta}(x,y;\sigma,\lambda,\omega)$, the linear orientation space representation $O(x,y,\theta)$ is defined as the filter response at the orientation θ, and is given by

$$O(x,y,\theta)=\int\int f^{\theta}(x-\xi,y-\eta;\sigma,\lambda,\omega)I(\xi,\eta)d\xi d\eta. \quad (4)$$

Property 1. *In accordance with the even symmetry of the filter, $O(x,y,\theta)$ is a periodic with period π, that is, this means that lines can only be represented over π orientations.*

Property 2. *$O(x,y,\theta)$ is continuous along the orientation axis θ according to*

$$\lim_{\varepsilon\to 0}O(x,y,\theta-\varepsilon)=\lim_{\varepsilon\to 0}O(x,y,\theta+\varepsilon)=O(x,y,\theta). \quad (5)$$

Consequently, the multiple orientation feature at each pixel in a given $I(x,y)$ is continuous along the orientation axis θ.

3 Multiple Orientation Line Segmentation in Orientation Space

In this section, we address the optimization of the scale and orientation parameters by which the filter is tuned to optimally fit the width and orientation of a line, outline

orientation space filtering for junction segmentation, solve curve grouping by orientation space filtering and, finally, we show how orientation space filtering is implemented.

3.1 Optimizing Scale and Orientation of Gabor Filter

In order to enhance a line characterized by width and orientation, we begin by tuning the filter to the optimum scale corresponding to the width of the line and then deal with the orientation using the filter tuned to fit the line width.

Let us consider an ideal line model whose profile has a Gaussian shape is given by

$$I(x,y;\sigma_L)=\exp\left(-\frac{x^2}{2\sigma_L^2}\right), \tag{6}$$

where σ_L is the standard deviation of the profile.

The filter response $R(x,y;\sigma,\lambda,\omega,\sigma_L)$ is given by

$$R(x,y;\sigma,\lambda,\omega,\sigma_L)= \frac{\sigma_L}{\sqrt{\sigma_L^2+\sigma^2}}\exp\left\{-\frac{x^2+4\pi^2{\sigma_L}^2\sigma^2\omega^2}{2(\sigma^2+{\sigma_L}^2)}\right\}\cos\left(\frac{2\sigma^2\pi\omega x}{\sigma^2+{\sigma_L}^2}\right). \tag{7}$$

We assume the following constraint condition: $\sigma\omega=C$, where $C=0.5$ in our experiments. The condition under which $R(x,y;\sigma,\lambda,\omega,\sigma_L)$ has a maximum of 1 at $x=0$ for a fixed σ_L is thus

$$\sigma_{opt}=\sqrt{4\pi^2C^2-1}\sigma_L. \tag{8}$$

The filter having the optimum scale corresponding to the line width is thus obtained by (8).

The filter (shown in (1)) is normalized as follows:

$$f^{\theta}(x,y;\sigma,\lambda,\omega)=\frac{\omega}{\sigma\lambda}\exp\left\{-\frac{\lambda^2x'^2+y'2}{2\sigma^2\lambda^2}+\frac{1}{2}\right\}\cos(2\pi\omega x'), \tag{9}$$

where $(x',y')=(x\cos\theta+y\sin\theta,-x\sin\theta+y\cos\theta)$. If lines having the same height but different widths were given, the filter responses have the same height using the normalized filter (shown in (9)). Therefore, multiple scale integration can be carried out using the normalized filter. We assume that the filter is tuned so as to have the optimal scale and to be normalized as below.

An ideal oblique line is obtained as follows by rotating (6) with an angle θ_1:

$$I^{\theta_1}(x,y;\sigma_L)=\exp\left\{-\frac{(x\cos\theta_1+y\sin\theta_1)^2}{2\sigma_L^2}\right\}. \tag{10}$$

The filter response $R(x,y,\theta;\theta_1,\sigma,\lambda,\omega,\sigma_L)$ of the oblique line (10) at an orientation θ, is thus given by

$$\begin{aligned}&R(x,y,\theta;\theta_1,\sigma,\lambda,\omega,\sigma_L)\\&=\frac{\pi\omega}{\sigma\lambda\sqrt{ad}}I^{\theta_1}(x,y;\sigma_L)\\&\exp\left\{\frac{l^2\cos^2\theta_1}{4a}-\frac{\pi^2\omega^2\cos^2\theta}{a}-\frac{f^2-g^2}{4d}+\frac{1}{2}\right\}\\&\cos\left(\frac{\omega\pi l\cos\theta\cos\theta_1}{a}+\frac{fg}{2d}\right),\end{aligned} \tag{11}$$

where

$$\begin{aligned}a(\theta)&=\frac{\lambda^2\cos^2\theta+\sin^2\theta}{2\sigma^2\lambda^2}+\frac{\cos^2\theta_1}{2\sigma_L^2},\\b(\theta)&=\frac{(\lambda^2-1)\sin2\theta}{2\sigma^2\lambda^2}+\frac{\sin2\theta_1}{2\sigma_L^2},\\c(\theta)&=\frac{\lambda^2\sin^2\theta+\cos^2\theta}{2\sigma^2\lambda^2}+\frac{\sin^2\theta_1}{2\sigma_L^2},\\d(\theta)&=c-\frac{b^2}{4a},l(x,y)=\frac{x\cos\theta_1+y\sin\theta_1}{2\sigma_L^2},\\f(\theta)&=2\pi\omega\left(\sin\theta-\frac{b}{2a}\cos\theta\right),\end{aligned}$$

and

$$g(x,y,\theta)=l\left(\sin\theta_1-\frac{b}{2a\cos\theta_1}\right).$$

There are three properties in $R(x_l,y_l,\theta;\theta_1,\sigma,\lambda,\omega,\sigma_L)$ where $x_l\cos\theta_1+y_l\sin\theta_1=0$ and Ω is the orientation bandwidth of the filter (3):

Property 3. *When $\theta=\theta_1$, the filter response*

$$R(x_l,y_l,\theta;\theta_1,\sigma,\lambda,\omega,\sigma_L)$$

has a maximum of 1 at each point (x_l,y_l).

Property 4. *The filter response at an orientation $\theta_1^-=\theta_1-\theta'$ $(\theta_1^-\in[\theta_1-\frac{\Omega}{2},\theta_1))$ is symmetry with respect to that at another orientation $\theta_1^+=\theta_1+\theta'$ $(\theta_1^+\in(\theta_1,\theta_1+\frac{\Omega}{2}])$, that is,*

$$R(x_l,y_l,\theta_1^-;\theta_1,\sigma,\lambda,\omega,\sigma_L)=R(x_l,y_l,\theta_1^+;\theta_1,\sigma,\lambda,\omega,\sigma_L). \tag{12}$$

Property 5. *If $\theta'\in[\theta_1-\frac{\Omega}{2},\theta_1+\frac{\Omega}{2}]$ and $\theta''\notin[\theta_1-\frac{\Omega}{2},\theta_1+\frac{\Omega}{2}]$*

$$R(x_l,y_l,\theta';\theta_1,\sigma,\lambda,\omega,\sigma_L)\gg R(x_l,y_l,\theta'';\theta_1,\sigma,\lambda,\omega,\sigma_L). \tag{13}$$

3.2 X- and T-Junctions in Orientation Space

Fig. 3a shows an oblique line and its filter response along the orientation axis θ at the center of the oblique line profile, and Fig. 3b and Fig. 3c depict X- and T-junctions and their filter responses along the orientation axis θ at the intersection centers of the X- and T-junctions, where the scale parameter σ of the filter is tuned as the optimum scale corresponding to the widths of the lines shown in Fig. 3. As shown in Fig. 3a, there is a local maximum corresponding to the orientation of the oblique line in the filter response. Fig. 3b and Fig. 3c show that, when the angle between the two lines at the X- or T-junction intersection is large, two local maxima, corresponding to each line segment orientation at the intersection, are detected in the filter response. Hence, the multiple orientations at the junction intersection centers can be represented and extracted in the orientation space.

We use mathematical line models to analytically define an ideal X-junction as:

$$\begin{aligned}X(x,y;\theta_X,\sigma_L)=&s\big(I^{\theta_1}(x,y;\sigma_L)-I^{\theta_2}(x,y;\sigma_L)\big)I^{\theta_1}(x,y;\sigma_L)\\&+s\big(I^{\theta_2}(x,y;\sigma_L)-I^{\theta_1}(x,y;\sigma_L)\big)I^{\theta_2}(x,y;\sigma_L),\end{aligned} \tag{14}$$

and an ideal T-junction as:

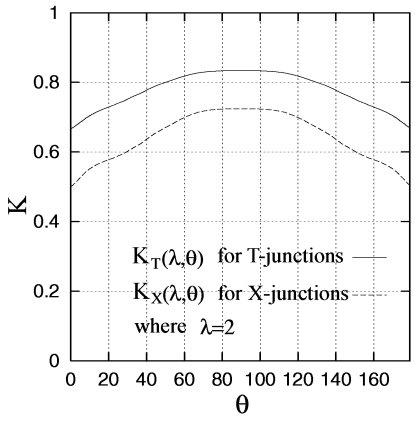

Fig. 2. Estimated coefficients $K_X(\lambda,\theta)$ for X-junctions and $K_T(\lambda,\theta)$ for T-junctions. Here, $\lambda = 2$.

$$T(x,y;\theta_T,\sigma_L) = s\big(I^{\theta_1}(x,y;\sigma_L) - I_s^{\theta_2}(x,y;\sigma_L)\big)I^{\theta_1}(x,y;\sigma_L) + s\big(I_s^{\theta_2}(x,y;\sigma_L) - I^{\theta_1}(x,y;\sigma_L)\big)I_s^{\theta_2}(x,y;\sigma_L), \quad (15)$$

where θ_X and θ_T given by $|\theta_1 - \theta_2|$ are the angles between the two lines at the X- and T-junction intersections, respectively, $I^{\theta}(x,y;\sigma_L)$ is given in (10), $I_s^{\theta}(x,y;\sigma_L)$ is defined as:

$$I_s^{\theta}(x,y;\sigma_L) = \exp\left\{-\frac{(x\cos\theta + y\sin\theta)^2}{2\sigma_L^2}\right\}$$

for $y \geq 0$, $I_s^{\theta}(x,y;\sigma_L) = 0$ for $y < 0$, and $s(x)$ is defined as $s(x) = 1$ for $x > 0$, $s(x) = \frac{1}{2}$ for $x = 0$, $s(x) = 0$ for $x < 0$.

Coefficients $K_X(\lambda,\theta_X)$ for an X-junction $X(x,y;\theta_X,\sigma_L)$ and $K_T(\lambda,\theta_T)$ for a T-junction $T(x,y;\theta_T,\sigma_L)$ can be certainly found (given in Fig. 2), thus the filter response $O(c_x,c_y,\theta)$ at the intersection center (c_x,c_y) of an X-junction or a T-junction in the orientation space can be approximately expressed as:

$$O(c_x,c_y,\theta) \approx \begin{cases} K_X(\lambda,\theta_X)(R(c_x,c_y,\theta;\theta_1,\sigma,\lambda,\omega,\sigma_L) \\ \quad +R(c_x,c_y,\theta;\theta_2,\sigma,\lambda,\omega,\sigma_L)), & \text{for an X -junction} \\ K_T(\lambda,\theta_T)(R(c_x,c_y,\theta;\theta_1,\sigma,\lambda,\omega,\sigma_L) \\ \quad +\frac{1}{2}R(c_x,c_y,\theta;\theta_2,\sigma,\lambda,\omega,\sigma_L)), & \text{for a T-junction,} \end{cases} \quad (16)$$

where $R(x,y,\theta;\theta',\sigma,\lambda,\omega,\sigma_L)$ is given in (11).

There are three properties in $O(c_x,c_y,\theta)$.

Property 6. *If the angle θ_X or θ_T (given by $|\theta_1 - \theta_2|$) is greater than a permissible value θ^*, the filter response $O(c_x,c_y,\theta)$ has bimodality, that is, there are two local maxima at θ_1 and θ_2, respectively, a local minimum exists at $\frac{\theta_1+\theta_2}{2}$ midway between the two local maxima. In addition, the difference between the local maxima and the local minimum in the case of X-junctions, or the difference between the smaller of the local maxima and the local minimum in the case of T-junctions becomes larger as θ_X or θ_T becomes larger (also illustrated in Fig. 3b and Fig. 3c).*

Property 7. *The filter responses $O(c_x,c_y,\theta)$ at orientations $\theta_1^- = \theta_1 - \theta'$ $(\theta_1^- \in [\theta_1 - \frac{\Omega}{2}, \theta_1))$ and $\theta_2^- = \theta_2 - \theta'$ $(\theta_2^- \in [\theta_2 - \frac{\Omega}{2}, \theta_2))$ are symmetry with respect to those at other orientations $\theta_1^+ = \theta_1 + \theta'$ $(\theta_1^+ \in (\theta_1, \theta_1 + \frac{\Omega}{2}])$ and $\theta_2^+ = \theta_2 + \theta'$ $(\theta_2^+ \in (\theta_2, \theta_2 + \frac{\Omega}{2}])$ respectively, that is,*

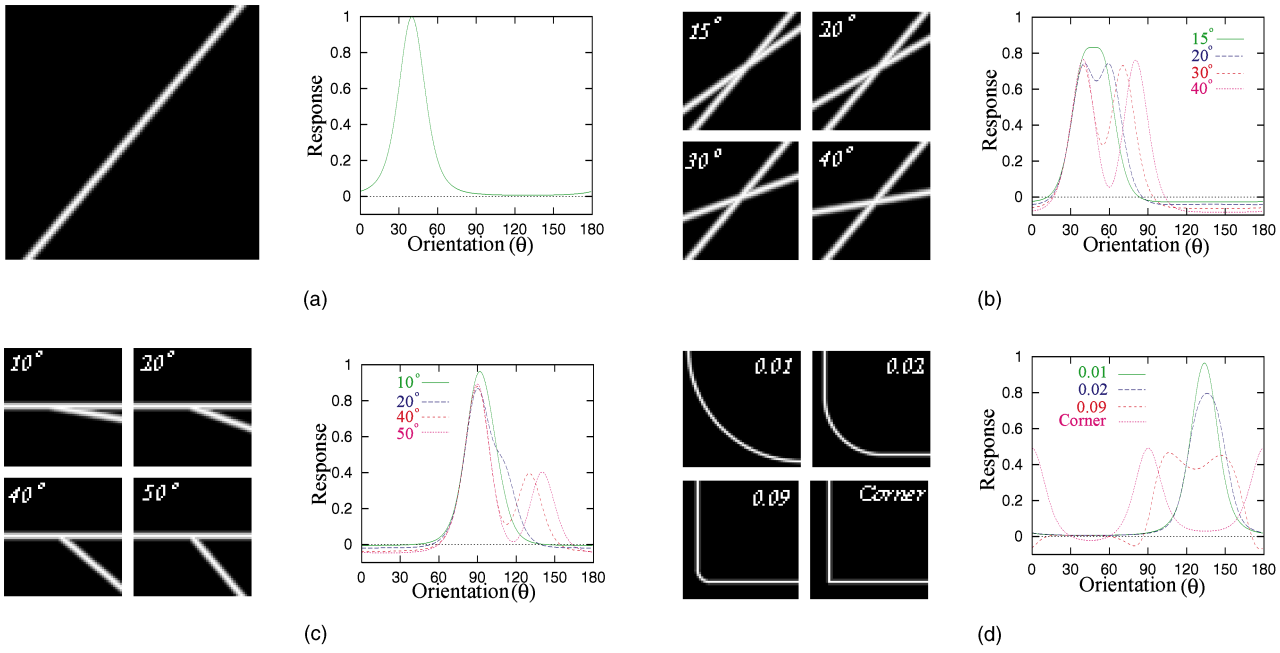

Fig. 3. (a) An oblique line, (b) , (c), and (d) X-, T-, and L-junctions, with their filter responses along the orientation axis θ at the center of oblique line profile, at the intersection centers of X-junctions at which the angle between two lines at each intersection is $15°, 20°, 30°$, or $40°$ and T-junctions at which the angle between two lines at the intersection is $10°, 20°, 40°$, or $50°$, and at the midpoints of the circular arcs at which the normalized curvature are $0.01, 0.02, 0.09$, and ∞ at L-junctions. Here, the filter response can be considered as a function of the orientation θ.

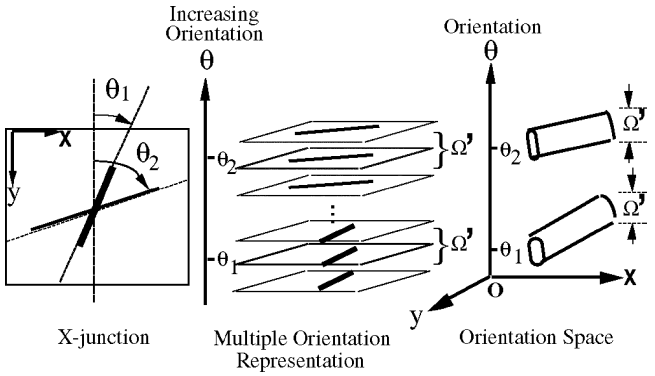

Fig. 4. Outline of the concept of orientation space filtering.

$$\begin{aligned} O(c_x, c_y, \theta_1^-) &= O(c_x, c_y, \theta_1^+) \\ O(c_x, c_y, \theta_2^-) &= O(c_x, c_y, \theta_2^+), \end{aligned} \tag{17}$$

where Ω is the orientation bandwidth of the filter (3).

Property 8. *Let (x, y) be a point at a junction intersection and $\theta_i (i \geq 1)$ be multiple orientations at the point (x, y). If $|\theta_i - \theta_j| > \theta^* (i \neq j)$, then each point of $(x, y, \theta_i)(i \geq 1)$ in the orientation space $O(x, y, \theta)$ satisfies:*

$$\begin{cases} \frac{\partial}{\partial \theta} O(x, y, \theta)\Big|_{\theta=\theta_i} = 0 \\ \frac{\partial^2}{\partial \theta^2} O(x, y, \theta)\Big|_{\theta=\theta_i} > 0, & \text{for dark lines} \\ \frac{\partial^2}{\partial \theta^2} O(x, y, \theta)\Big|_{\theta=\theta_i} < 0, & \text{for light lines.} \end{cases} \tag{18}$$

As depicted in Fig. 4, which outlines the concept of orientation space filtering, one line at a given X-junction is inclined at an orientation θ_1 and the other line at another orientation θ_2. When we continuously tune the filter along the orientation axis θ at increments of $\triangle\theta$ (we used $\triangle\theta = 1^\circ$ in our experiments) to filter the X-junction in the orientation space, in accordance with the orientation resolution of the filter, the filter responses show relatively large magnitudes within $[\theta_1 - \frac{\Omega'}{2}, \theta_1 + \frac{\Omega'}{2}]$ and $[\theta_2 - \frac{\Omega'}{2}, \theta_2 + \frac{\Omega'}{2}]$—where $\Omega' \leq \Omega$—at the orientation axis θ, and have two local maxima at the orientation θ_1 and θ_2 in the orientation space. According to **Properties 6** and **7**, if $|\theta_1 - \theta_2| > \theta^*$, each line extracted by filtering in the orientation space can form a connected component therein and there is a one-to-one correspondence between each connected component in the orientation space and each line. By virtue of the continuity of the filter response and the orientation selectivity of the filter, the connected components in the orientation space are easily separated using a threshold which is selected between the local minimum and local maxima in the filter response. Consequently, we can treat the problem of multiple orientation line segmentation as one of detecting the connectivity in the orientation space.

The limit in the permissible value θ^* of the angle between the two lines at the intersection of an X-junction, as well as of a T-junction, depends upon the orientation bandwidth Ω of the filter and is regarded as the sensitivity limit of our proposed method for X- and T-junction segmentation. The behavior of the method with respect to the limitation in the value of the angle between the two lines at X- and T-junction intersections when the orientation bandwidth of the filter is varied is demonstrated in Section 4 by means of a simulation analysis using mathematical line models.

3.3 Intersecting Curves in Orientation Space

A 2D smooth curve $\vec{\gamma}(s)$ is parameterized by the arc length s: $\vec{\gamma}(s) = (x(s), y(s))$, where $s \in [0, L]$. The winding angle $\theta(s)$ along the arc length s is defined as the cumulative angle described by the tangent when the curve advances from $s = 0$ to $s = L_1$ and is regarded as a continuous function of the arc length s owing to the smoothness of the curve.

By treating the winding angle $\theta(s)$ as a controlled orientation parameter along the arc length s and embedding $\vec{\gamma}(s)$ with the filter $f^{\theta(s)}(x, y; \sigma, \lambda, \omega)$—which is continuously tuned to the winding angle $\theta(s)$—into the orientation space, the orientation space representation $O(x(s), y(s), \theta(s))$ of $\vec{\gamma}(s)$ can be obtained. By virtue of the continuity of the winding angle $\theta(s)$, $O(x(s), y(s), \theta(s))$ is a continuous function with respect to the arc length s and the curve $\vec{\gamma}(s)$ can be projected as $O(x(s), y(s), \theta(s))$ in the orientation space. Consequently, in the orientation space, a connected component originating from the curve $\vec{\gamma}(s)$ can be formed and the path of the curve $\vec{\gamma}(s)$ along the arc length s is continuous to enable tracking in the connected component. From our conclusion that each connected component uniquely corresponds to the respective position in the global geometry of each curve and groups the orientation and curvature continuities of each curve, the global discontinuity arising from intersecting curves can be dissolved in the orientation space, that is, intersecting curves can be separated and segmented in the orientation space. Therefore, curve grouping can be achieved by orientation space filtering.

Since filtering a curve in the orientation space is a special process that represents a curve as a sequence of line segments, that is, tangent line segments at the winding angle $\theta(s)$ along the arc length s, the sensitivity to a curve having a high degree of curvature is low when the orientation selectivity of the filter is high. For this reason, the curvature of a curve influences the curve segmentation performance. We employ an L-junction—which has circular arcs with a normalized curvature κ_L and is analytically defined as a mathematical line model in the Appendix—to locally analyze the sensitivity of our method to the normalized curvatures of curves. Fig. 3d depicts L-junctions with their filter responses along the orientation axis θ at the midpoints of the circular arcs. As depicted in the figure, when κ_L is large, two local maxima are detected in the filter response, the L-junction is then fragmented into two line segments; on the other hand, when κ_L is small, only one local minimum is detected in the filter response and the L-junction is segmented according to its orientation and curvature continuities. Unlike the cases of X-junctions, T-junctions, and corner segmentation, a filter response having only one maximum is desirable for the segmentation of an L-junction having a relatively small κ_L.

The performance of the curve segmentation method and the relationship between its sensitivity to curvature and the orientation selectivity of the filter are discussed in Section 4 by means of a simulation analysis using L-junctions.

TABLE 1
Minimal Angle θ_X, Minimal Angle θ_T, and Maximal Normalized Curvature κ_L when $\lambda = 1, 2, 3, 4, 5$

λ	Minimal θ_X	Minimal θ_T	Maximal κ_L
1	57°	48°	0.14
2	28°	26°	0.09
3	19°	17°	0.03
4	15°	13°	0.02
5	12°	11°	0.01

3.4 Implementation of Orientation Space Filtering

The implementation of the proposed method for segmenting and separating multiple orientation lines can be summarized as follows:

1. After filtering the image in the orientation space, thresholding is performed to obtain the connected components. The result of thresholding is represented by

$$O_T(x,y,\theta) = \begin{cases} S(O(x,y,\theta) - T_1), & \text{for light lines} \\ S(T_1 - O(x,y,\theta)), & \text{for dark lines,} \end{cases} \tag{19}$$

   where T_1 is the threshold and $S(x)$ is defined as $S(x) = 1$ for $x > 0$, otherwise $S(x) = 0$. The connected components in $O_T(x,y,\theta)$ can be considered to correspond to each segmented line.
2. Labeling is then carried out for the connected components in $O_T(x,y,\theta)$. Let the result of labeling be $O_L(x,y,\theta)$. While the noise components are suppressed by orientation space filtering, some noise components may still remain. However, these components will be removed by thresholding because their volume should be small. Let l^i be the set of pixels in an image that compose a line i. Then, each l^i is segmented by mapping the points with the same label in the orientation space to a 2D image plane. That is,

$$l^i \in \{(x,y) | (O_L(x,y,\theta) = i), \text{and } V_i > T_2\}, \tag{20}$$

   where i denotes the number of connected components labeled in $O_L(x,y,\theta)$ corresponding to l_i, V_i is the number of voxels of the connected components labeled i, and T_2 is the threshold.

4 Sensitivity Analysis Using Mathematical Simulations

4.1 Sensitivity Limits for Segmentation of Junctions

The orientation bandwidth of the filter decisively affects the sensitivity limit of the method. As indicated in (3), the orientation bandwidth Ω depends upon the filter parameters: σ, ω, and λ. Since we assumed that $\sigma\omega = C$, Ω is inversely proportional to λ. Therefore, if λ is large, Ω is small, that is, the orientation selectivity is high. Experimental simulations for segmenting X-, T-, and L-junctions were performed by changing λ, the angle θ_X at an X-junction intersection, the angle θ_T at a T-junction intersection, and the normalized curvature κ_L of the circular arc at an L-junction, respectively.

As described above, the threshold T_1 (19) is selected so as to be between the local maxima and local minimum midway between the local maxima in the filter response at an X-junction intersection center, as well as between the smaller of the local maxima and local minimum midway between the local maxima in the filter response at a T-junction intersection center along the orientation axis θ. In order to be able to reliably segment lines at multiple orientations, it is desirable to have a relatively wide range within which the threshold T_1 can be selected. Based on the results of experimental simulations, we computed the minimal θ_X at an X-junction intersection where the local minimum is less than half of the local maxima, the minimal θ_T at a T-junction intersection where the local minimum is less than half of the smaller of the local maxima, and the maximal κ_L at an L-junction where the filter response has only one local maximum, for $\lambda = 1, 2, 3, 4$, and 5. Table 1 illustrates the computed results. As given in the table, when λ becomes larger, the values of minimal θ_X and θ_T at X- and T-junctions that can be separated and segmented become small, that is, the sensitivity of the method for segmenting X- and T-junctions becomes higher. On the other hand, if λ is small, the maximal κ_L at an L-junction that can be stably segmented with its orientation and curvature continuities becomes larger, that is, the sensitivity to high degree of curvature becomes higher, while the orientation selectivity becomes lower as λ becomes smaller.

Taking account of the behavior characteristics of the minimal angles θ_X, θ_T and the maximal curvature κ_L in our subsequent experiments, we employed $\lambda = 2$ to achieve a good trade-off between sensitivity and selectivity.

4.2 Influences of Selecting Filter Scales on Sensitivity to Segmentation of Junctions

We have tuned the scale parameter σ of the filter as the optimum scale fitting the width of a line (8). In order to reveal the influences of selecting the filter scale σ on the sensitivity to segmentation of X-, T-, and L-junctions, we continuously treat the orientation parameter θ and the scale parameter σ of the filter to construct an orientation-scale space, and then investigate the sensitivity variations therein.

As illustrated in Fig. 5 (first column and second column), in the orientation-scale space, two local maxima corresponding to two orientations at the intersection center of the X- or T-junction are detected along the orientation axis θ at each scale σ. Fig. 5 (third column) shows that the magnitude in the filter response $R(\sigma)$ corresponding to the local maximum R

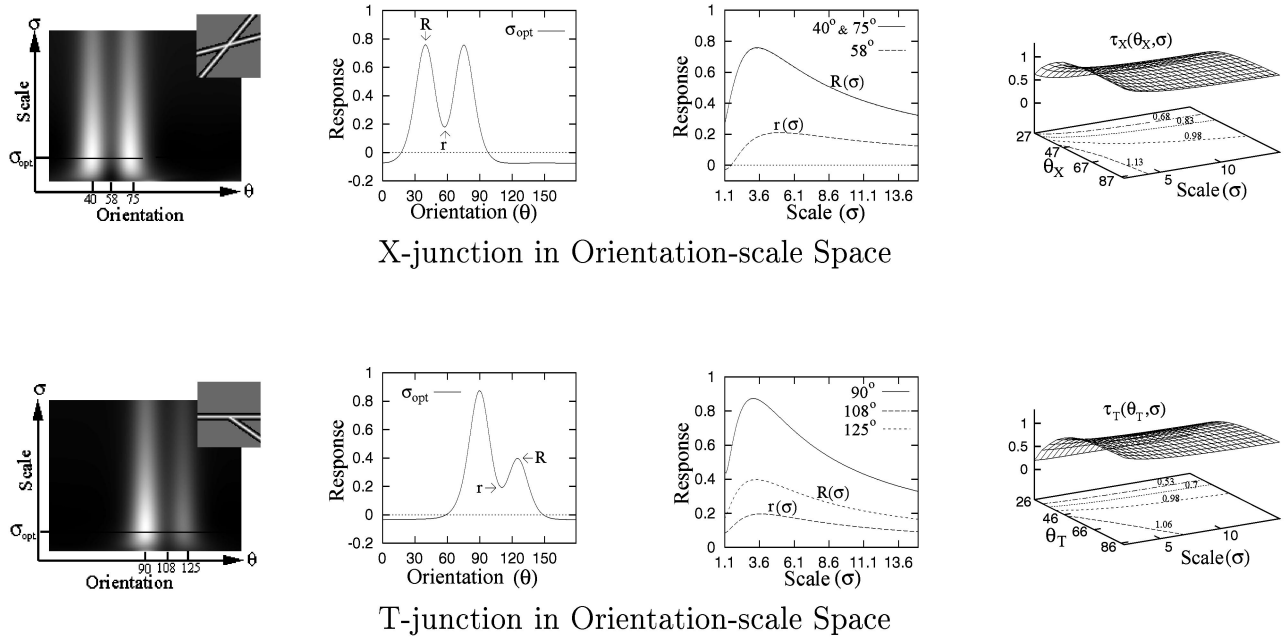

Fig. 5. (First column from left): The filter responses in the orientation-scale space at the intersection centers of an X-junction—at which one line is inclined at $40°$, the other line at $75°$—and a T-junction—at which one line is inclined at $90°$, the other line at $125°$. Here, each filter response is represented by an intensity image. (Second column): The filter responses at the optimum scales σ_{opt} along the orientation axis θ at the X- and T-junction intersections. (Third column): The filter responses at the X- and T-junction intersection centers along the scale axis σ at the three orientations at which the two local maxima and the local minimum between them are detected in the filter response along the orientation axis θ; here, the three orientations are $40°$, $75°$, and $58°$ in the case of the X-junction and are $90°$, $108°$, and $125°$ in the case of the T-junction. (Fourth column): Two 3D-plots representing $\tau_X(\theta_X, \sigma)$ and $\tau_T(\theta_T, \sigma)$ and their contour lines at the θ_X-σ and θ_T-σ planes.

in Fig. 5 (second column) is greater than that in the other filter response $r(\sigma)$ corresponding to the local minimum r in Fig. 5 (second column) over the scale axis σ. Therefore, the X-and T-junctions can be segmented by the threshold T_1 (19), whose range is wide, over the scale axis σ. If an X-junction with θ_X, a T-junction with θ_T, and a scale σ were given, we respectively let the local maxima in the filter response at the X-junction intersection and the smaller of the two local maxima in the filter response at the T-junction intersection along the orientation axis θ at the scale σ be $R_X(\theta_X, \sigma)$ and $R_T(\theta_T, \sigma)$ and the local minimum midway between the local maxima at the X- and T-junction intersection be $r_X(\theta_X, \sigma)$ and $r_X(\theta_T, \sigma)$. We define two criterions $\tau_X(\theta_X, \sigma)$ as: If $r_X(\theta_X, \sigma)$ exists,

$$\tau_X(\theta_X, \sigma) = 1 - \frac{r_X(\theta_X, \sigma)}{R_X(\theta_X, \sigma)},$$

otherwise $\tau_X(\theta_X, \sigma) = 0$, and $\tau_T(\theta_T, \sigma)$ as: if $r_T(\theta_T, \sigma)$ exists

$$\tau_T(\theta_T, \sigma) = 1 - \frac{r_T(\theta_T, \sigma)}{R_T(\theta_T, \sigma)},$$

otherwise $\tau_T(\theta_T, \sigma) = 0$, to evaluate the sensitivity to segmentation of X- and T-junctions by varying θ_X, θ_T, and σ. If $\tau_X(\theta_X, \sigma)$ or $\tau_T(\theta_T, \sigma)$ is larger, the two lines—which have an intersection angle θ_X at an X-junction, or an intersection angle θ_T at a T-junction—can be separated by the threshold T_1 having a relatively wide range. Fig. 5 (fourth column) shows two 3D-plots and their contour lines illustrating $\tau_X(\theta_X, \sigma)$ and $\tau_T(\theta_T, \sigma)$. As illustrated in the figure, when $\theta_X > 28°$ and $\theta_T > 26°$, both $\tau_X(\theta_X, \sigma)$ and $\tau_T(\theta_T, \sigma)$ are greater than 0.5. Therefore, the sensitivity to segmentation of X- and T-junctions is independent of the tuned filter scale σ, while the magnitude in filter response becomes smaller as σ becomes larger.

Fig. 6 (first column and second column) show the filter response at the midpoint of a circular arc in an L-junction in the orientation-scale space and two filter responses at the optimum scale σ_{opt} and a large scale σ_L along the orientation axis θ, respectively. As depicted in the figures, only one local maximum is detected in the filter responses at σ_{opt}, as well as small scales along the orientation axis θ; however, two local maxima are detected in filter responses at large scales such as σ_L, that is, if σ is large, the L-junction should be fragmented as two segments. In case that two local maxima are detected in the filter response along the orientation axis θ, we let the local maxima be $R_L(\kappa_L, \sigma)$, and the local minimum between the two local maxima be $r_L(\kappa_L, \sigma)$. We also define a criterion $\tau_L(\kappa_L, \sigma)$ as: If $r_L(\kappa_L, \sigma)$ exists,

$$\tau_L(\kappa_L, \sigma) = 1 - \frac{r_L(\kappa_L, \sigma)}{R_L(\kappa_L, \sigma)},$$

otherwise $\tau_L(\kappa_L, \sigma) = 0$, to evaluate the sensitivity to segmentation of L-junctions by varying κ_L and σ. If $\tau_L(\kappa_L, \sigma) = 0$, the L-junctions can be segmented; if $\tau_L(\kappa_L, \sigma) > 0$, the L-junctions should be fragmented into two segments. Fig. 6 (third column) gives a 3D-plot illustrating $\tau_L(\kappa_L, \sigma)$. As illustrated in the figure, the range of scale σ where $\tau_L(\kappa_L, \sigma) = 0$ becomes narrower as κ_L becomes larger. Again, for a large κ_L, the sensitivity to L-junction segmentation becomes lower, that is, $\tau_L(\kappa_L, \sigma) > 0$, as σ becomes larger. Therefore, the sensitivity

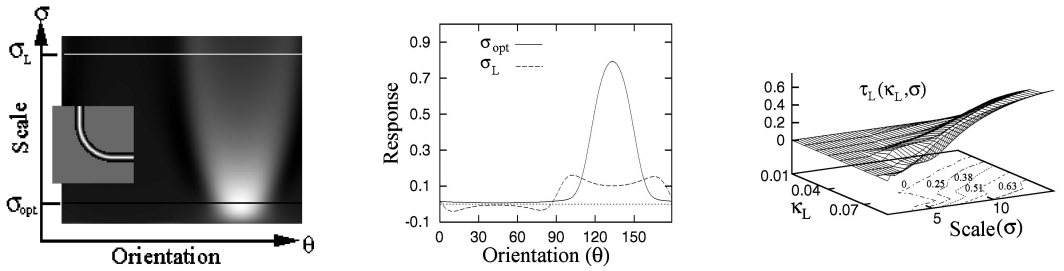

Fig. 6. (Left): An L-junction with a circular arc and the filter response at the midpoint of the circular arc in the orientation-scale space, where $\kappa_L = 0.04$. (Middle): The filter responses at the optimum scale σ_{opt} and a large scale σ_L along the orientation axis θ. (Right): A 3D-plot representing $\tau_L(\kappa_L, \sigma)$ and its contour line at the κ_L-σ plane.

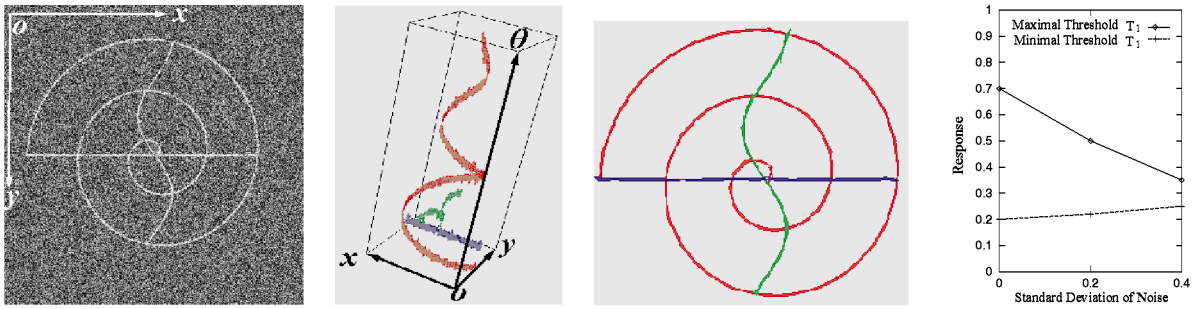

Fig. 7. (a) Synthesized image of three intersecting curves with additive Gaussian noise. The image consist of a sinusoidal curve, an Archimedes spiral, and a horizontal line. (b) Three connected components corresponding to the two curves and line extracted in the orientation space and colored. The θ-axis is the orientation axis; the x- and y-axes correspond to the x- and y-axes in (a). (c) The three curves segmented by orientation space filtering and colored. (d) Two plots giving the minimal and the maximal threshold for the topology shown in (b) when the standard deviation of additive Gaussian noise is varied from 0 to 0.4 in increments of 0.2.

to L-junction segmentation depends upon the normalized curvature κ_L and the tuned scale σ of filter.

5 Experimental Results

5.1 Synthesized Image

We synthesized an image including a sinusoidal curve and a spiral, as well as a line—where the height of each line profile is 1, and $\sigma_L = 1$—and imposed additive Gaussian noise with the standard deviation σ_n of 0.4 and a mean of 0 on it. Fig. 7a shows the synthesized image. Along the arc length s of the spiral, the normalized curvature $\kappa(s)$ of the spiral varies continuously and, from the periphery to the center, the winding angle $\theta(s)$ of the spiral continuously varies from $0°$ to $900°$. There are a number of X-junctions with different angles θ_X and T-junctions with different angles θ_T at the intersections. In order to cover all the winding angles of the spiral, we constructed the orientation space of the image where the orientation variable θ is set from $0°$ to $900°$. In constructing the orientation space, based on **Property 1** that the orientation space representation $O(x, y, \theta)$ is a periodic with period $180°$, we continuously filtered the image by dealing with the orientation parameter from $0°$ to $180°$ at increments of $1°$ and then assigned the filtered results to the orientation space. Fig. 7b depicts the spiral, curve, and line in the orientation space and shows that, after filtering, the three connected components, which group the orientation and curvature continuities of the two curves and the line in the orientation space, respectively, were separated and then obtained in the orientation space. The global discontinuities were also dissolved by the connected components. It should be particularly noted that, by virtue of the winding angle $\theta(s)$ with respect to the arc length s of the spiral, the connected component (colored red in Fig. 7b) arising from the spiral advances spirally in the orientation space. Fig. 7c shows the result of segmentation; it can be seen that the two curves and the line were segmented out by orientation space filtering. Fig. 7d gives the maximal and minimal thresholds between which the spiral, curve, and line are segmented out to obtain the topology shown in Fig. 7b when the standard deviation of additive Gaussian noise imposed is increased from 0 to 0.4 in increments of 0.2. As demonstrated by the segmented acquired image, curve grouping and segmentation can be realized by orientation space filtering.

5.2 Real Images

5.2.1 Coronary Angiogram

Fig. 8a shows an X-ray coronary angiogram. There are several overlapping arteries in the left coronary. In Fig. 8b, the terminological abbreviations and ordering numbers of the main coronary arteries according to the American Heart Association classification are shown superimposed on the angiogram. As can be seen in the figure, arteries SEP2 and SEP3 intersect with D1 forming two X-junctions; LCX, D1, SEP2, and SEP3 connect to LAD forming three T-junctions; and AC, OM, PL-1, and PL-2 connect to LCX forming four T-junctions. In order to segment arteries in the coronary angiogram, we used $\sigma_L = 2.0$ to estimate the artery widths, and $C = 0.5$ and $\lambda = 2$ to construct the orientation space.

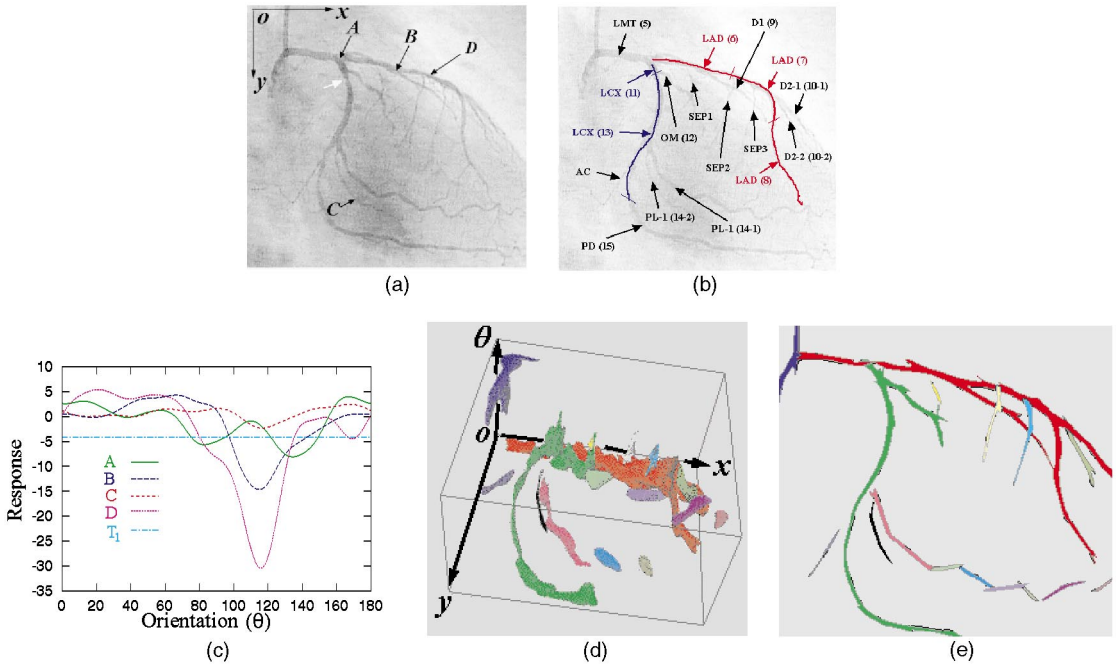

Fig. 8. (a) An X-ray coronary angiogram with several overlapping arteries. The points A, B, C, and D are referred to in (c). The white arrow indicates stenosis. (b) Abbreviations and ordering numbers of the main coronary arteries. (c) Filter responses at points A, B, C, and D marked in (a) along the orientation axis θ and threshold T_1. (d) Sixteen connected components were extracted and labeled in the orientation space. The θ-axis is the orientation axis; the x- and y-axes correspond to the x- and y-axes in (a). (e) Sixteen arteries or artery segments were segmented and labeled. Overlapping arteries in (a) were effectively separated.

According to the even symmetry of the filter, line structures can only be represented over 180° orientations. We therefore dealt with the orientation parameter θ from 0° to 180° at increments of 1° to cover all the orientations of the coronary arteries.

Fig. 8c shows the four filter responses along the orientation axis θ at the X-junction intersection A, the T-junction intersection B, point C in the distal segment of PL-2, and point D at which the gray-level is a great contrast to that at the nearby background shown in Fig. 8a. Local minima presented in the filter responses correspond to multiple orientations at each junction intersection in the coronary owing to dark arteries. In filter response A, two local minima corresponding to the two orientations at point A were detected; there is only one local minimum in filter response B due to the narrowness of the angle between D1 and LAD at their intersection; the absolute magnitude of the local minimum in filter response C is relatively small because the gray-level at point C is close to that at the nearby background; the absolute magnitude of the local minimum in filter response D is relatively large due to the greater difference in gray-level at point D and the nearby background. As can be seen in Fig. 8d, 16 connected components were extracted in the orientation space by selecting the threshold T_1 (19) shown in Fig. 8c and another threshold T_2 (20).

Fig. 8e indicates that the 16 coronary arteries or artery segments were effectively segmented, including arteries appearing as X- and T-junctions. In Fig. 8e, the main coronary arteries are seen to be well-detected by orientation space filtering, in contrast to their depiction in Fig. 8b. However, there are the following limitations in the segmentation of the coronary arteries (shown in Fig. 8e).

1. The branch structure between the arteries SEP1 and LAD is too complex to be segmented out for the three reasons: First, the root of SEP1 connects to the root of LAD forming a T-junction with a narrow intersection angle; second, the midsegment of SEP1 intersects the proximal segment of LAD, forming an X-junction which also has a narrow intersection angle; third, the width of SEP1 differs from that of LAD and the root of SEP1 is near LAD.
2. The arteries LAD and D1 at the T-junction B were detected, but they were not able to be separated because only one local minimum was detected in the filter response B shown in Fig. 8c.
3. The artery PL-1 was fragmented into seven segments due to the large magnitude of the normalized curvature at each of its inflection points.
4. The distal segment of artery PL-2 was not detected due to the small absolute magnitude of the local minimum in filter response at each of points therein (e.g., the filter response C shown in Fig. 8c).

5.2.2 Spatiotemporal Image of a Microvessel

Fig. 9a shows a microscopic image of a rat mesentery microvessel. In order to measure the motion of leukocytes flowing along the microvessel shown in Fig. 9a, we generated a spatiotemporal image whose spatial axis is parallel to the vessel region contour to visualize the motion of leukocytes flowing along a microvessel [27], [28]. A leukocyte, which is sphere-like and limited in diameter, is not as deformable as an erythrocyte. Also, the velocity of leukocytes is relatively limited. Hence, in a spatiotemporal

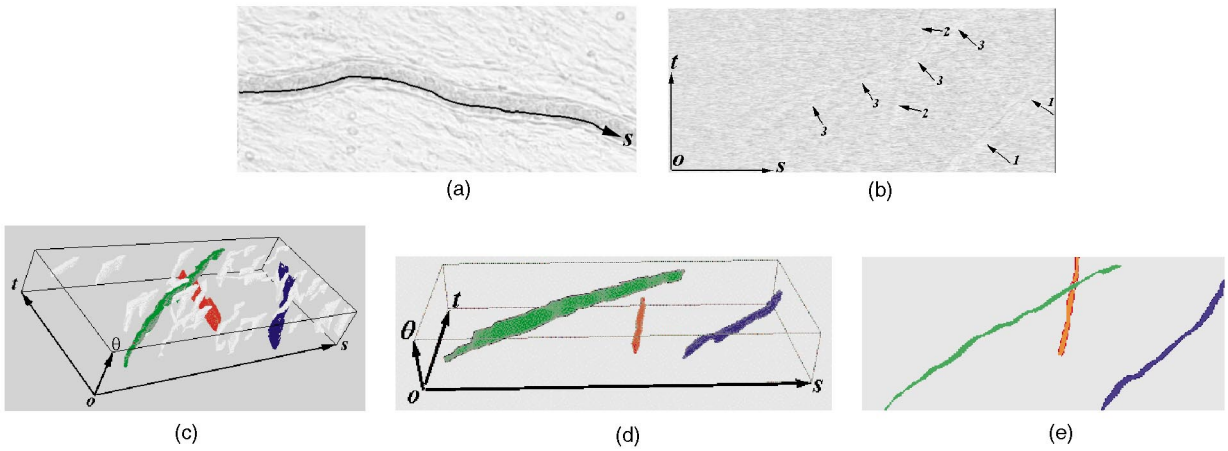

Fig. 9. (a) One frame from a microscopic image sequence of a rat mesentery microvessel. The spatial axis is denoted as the s-axis. (b) A spatiotemporal image of the microvessel in which there are three leukocyte traces appearing as dark lines and numbered. The t-axis is the temporal axis. (c) An interim result of orientation space filtering. Not only the three connected components corresponding to the three leukocyte traces, but also extra connected components (shown as white blocks) caused by noise were extracted by the threshold T_1 in the orientation space. (d) Three connected components corresponding to the three leukocyte traces were extracted in the orientation space. The θ-axis in (c) and (d) is the orientation axis; the s- and t-axes in (d) and (e) correspond to the s- and t-axes in (b). (e) The three leukocyte traces were segmented and labeled.

image, each leukocyte trace appears as a slanting linear structure that has a limited width corresponding to the diameter of the leukocyte and a relatively long length. Fig. 9b shows the spatiotemporal image. Three leukocyte traces can be seen. Since the leukocytes are obscured by many erythrocytes, in the spatiotemporal image the leukocyte traces suffer from erythrocyte interruption and are buried in the noise, making them difficult to identify clearly. Also, two of the leukocyte traces are shown as intersecting because one of the leukocytes has caught up with another one. To extract the leukocyte traces in the spatiotemporal image, we employed $\sigma_L = 2.0$ to estimate the widths of the traces and $C = 0.5$ and $\lambda = 2$ to construct the orientation space. Because the leukocyte velocity is limited, we dealt with the orientation parameter θ from 0° to 90° at increments of 1° to cover all the directions of the leukocyte traces.

Fig. 9c illustrates the interim result of orientation space filtering, in which connected components extracted in the orientation space by the threshold T_1 (19) can be seen. It is clear that the volumes of the connected components corresponding to the leukocyte traces are greater than the volumes of the connected components caused by noise. Fig. 9d shows the result of orientation space filtering by thresholding the interim result with the threshold T_2 (20) to remove the small connected components caused by noise. Three connected components corresponding to the three leukocyte traces were obtained in the orientation space. When these three traces were segmented (Fig. 9e), the motion of each individual leukocyte could be extracted and measured.

5.2.3 Scanned Japanese Character Image

Fig. 10 (the upper left of a, b, and c) show a scanned Japanese character at which the height of profile is 1 and the Japanese character scattered with additive Gaussian noise with a mean of 0 and standard deviation σ_n, where $\sigma_n = 0.5$, or 1.0. The Japanese character is made up of four overlapping strokes. We employed $\sigma_L = 2.0$ to estimate the widths of the strokes and dealt with the orientation parameter θ from 0° to 359° at increments of 1° to cover all the winding angles of the strokes. Fig. 10 (the upper right of a, b, and c) depicts the interim results of orientation space filtering. As depicted in the figures, several small connected components caused by noise components were extracted, while the connected components corresponding to the strokes in the Japanese character were obtained and separated in the interim results using the threshold T_1 (19). Fig. 10 (the lower left of a, b, and c) show, the final result of segmenting the Japanese character by orientation space filtering. The noise components were removed by the second threshold T_2 (20) and the connected components corresponding to the strokes in the Japanese character were extracted. As a result of these strategies, the strokes in the Japanese character with different levels of additive Gaussian noise were segmented and labeled (Fig.10 (the lower right of a, b, and c)). When $\sigma_n = 1$, the five connected components were obtained and then the longest arc-like stroke was fragmented into two segments, while the other strokes were segmented out.

6 Discussion and Conclusions

We have described a method for the segmentation of lines at multiple orientations using orientation space filtering. The sensitivity limits of the method were revealed using mathematical simulations. The influence of threshold selection on the reliability of segmentation was also discussed. Finally, the effectiveness of the method in segmenting lines at multiple orientations was demonstrated using a synthesized image and three real images.

Both scale and orientation are very informative features for early vision. The scale space concept introduced by Witkin [29] and subsequently explored in detail by Yuille and Poggio [30], Babaud et al. [31], and Lindeberg [32], [33], has been effectively applied as a feature space to

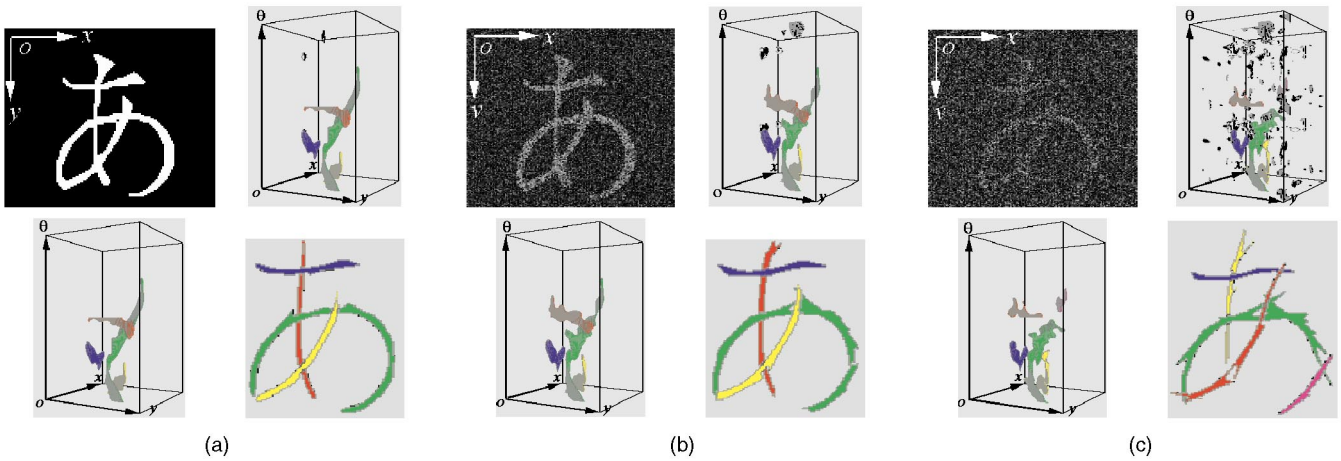

Fig. 10. (The upper left of (a), (b) and (c)): A scanned Japanese character and the Japanese character scattered with additive Gaussian noise with a mean of 0 and standard deviations σ_n, where σ_n is 0.5 or 1. (The upper right of (a), (b) and (c)): Interim results of orientation space filtering with the threshold T_1. Several small connected components (shown as dark blocks) caused by noise components were extracted, while four connected components for $\sigma_n = 0$ or 0.5 and five connected components for $\sigma_n = 1$ corresponding to the intersecting strokes in the Japanese character were obtained. (The lower left of (a), (b), and (c)): The result of orientation space filtering. The small connected components were removed by the other threshold T_2, therefore, the intersecting strokes were segmented and labeled (The lower right of (a), (b), and (c)). The θ-axis in the interim and final results is the orientation axis.

represent multiple scale features. In this paper, we focus on the orientation feature to characterize lines and employ the real component of a complex Gabor filter with even symmetry as our tunable filter. We then construct a feature space—"orientation space" to represent the multiple orientation features of lines by treating the orientation parameter as a continuous variable based on the tunable filter having orientation selectivity and a narrow orientation bandwidth. By virtue of the continuity, the problem of multiple orientation segmentation is formulated as one of finding the connectivity in the 3D orientation space. Therefore, there is a novelty in the method that the segmentation of lines at multiple orientations can be achieved by thresholding 3D images of the orientation space and then finding the connected components—which group the orientation and curvature continuities of lines, as well as curves, and dissolve the global discontinuities raising from intersecting curves and lines—therein. However, there is a drawback in the method that a great amount of computation cost is needed.

We will compare our proposed method with previously reported related methods in terms of orientation and junction analysis, and curve grouping and segmentation.

Orientation and Junction Analysis. In previous related work in the area of orientation and junction analysis, multiple orientation features at each pixel in an image have been detected by searching for local maximal responses with respect to orientation using steerable filters, and have been represented by polar plots [14], [15], [17], [18], [19]; to finally extract and segment junctions using these approaches, it is then necessary to apply extra tracking and grouping algorithms. Our method and previous work share certain similarities in that both utilize filters having sharp orientation selectivity to represent multiple orientation features at junctions in an image. However, unlike previous approaches, our method avoids the need to employ tracking algorithms to separate and segment junctions, because lines at multiple orientations are represented and then segmented by the connected components in the orientation space. The method is therefore both brief and powerful.

Curve Grouping and Segmentation. Previous approaches to curve grouping have adopted continuity, smoothness, and curvature constraints to estimate traces, curvatures, and tangents of curves [20], [21], [24]. Elder and Zucker [24] proposed employing an extended tangent representation to locally represent closure contours as a set of tangent vectors and then grouping the tangent vectors using a Bayesian model to realize contour grouping. Our method differs from these approaches in that no form of constraint or hypothesis is considered. Since each point on a curve originates from the global geometry of the curve and the winding angle varies continuously along the arc length, after being embedded into the orientation space by filtering, each curve can form a connected component therein. Consequently, curve grouping and segmentation can be concisely represented and realized in the orientation space.

Since multiple orientation line segmentation is accomplished by thresholding in the orientation space, the selection of the two thresholds T_1 and T_2 ((19) and (20)) also plays a key role in orientation space filtering. The first threshold, T_1, is selected so as to be between the local maxima and the local minimum midway between the local maxima in the filter response at an X-junction intersection center, as well as between the smaller of the local maxima and the local minimum midway between the local maxima in the filter response at a T-junction intersection center along the orientation axis θ. The connected components corresponding to the lines at the X-junction are obtained and separated in the orientation space by means of a suitably selected T_1; in particular, if the local minimum is less than half of the local maxima in the filter response, T_1

can be selected within a wide range. The threshold selection range is wide, which means that the sensitivity of the method for segmenting X- and T-junctions is high. The findings depicted in Fig. 7 showed that the efficient threshold range that can be used to segment junctions becomes narrower as the standard deviation of additive Gaussian noise becomes larger; however, even at higher standard deviations, some degree of threshold range could still be obtained. Since the scale parameter σ of the filter has been tuned so as to fit the width of the line (8) and the parameter λ is set relatively large ($\lambda = 2$) to give sharp orientation selectivity, many noise components should be suppressed by the filter and removed by the threshold T_1. However, as illustrated in the result (Fig. 10), not only the connected components corresponding to the strokes at the Japanese character but also connected components caused by noise will be extracted in the orientation space by the threshold T_1 if the additive Gaussian noise standard deviation becomes large. The second threshold T_2 thus is selected to effectively remove connected components that are caused by noise and have relatively small volumes in the orientation space. Our experimental results verified that lines at multiple orientations could be reliably segmented by selecting appropriate thresholds T_1 and T_2 in the orientation space.

Segmenting lines of various widths and orientations is very important and significant in early vision. With the aim of integrating multiple scale and orientation features of lines, we plan to develop multidimensional feature space, such as orientation-scale space filtering. Additionally, we believe our method has the potential to segment multiple edges and combinations of edges and lines by adding the imaginary component of the Gabor filter with odd symmetry to extend our tunable filter so that it has a quadrature pair and using the squared output of the quadrature pair of the extended tunable filter to construct the orientation space.

APPENDIX

L-JUNCTION LINE MODEL

The L-junction line model $L(x, y; c_x, c_y, r_L, \sigma_L)$, which has a circular arc with its center at (c_x, c_y), a radius r_L, and an angle $\frac{\pi}{2}$ at the circumference, is analytically given by

$$L(x, y; c_x, c_y, r_L, \sigma_L) = \begin{cases} \exp\left(-\frac{(x+r_L-c_x)^2}{2\sigma_L^2}\right) & ; y < c_y \\ \max_t\left\{\exp\left(-\frac{(x-c_x-r_L\cos t)^2+(y-c_y-r_L\sin t)^2}{2\sigma_L^2}\right)\right\} & ; x \le c_x, y \ge c_y, \\ & \text{and } \pi \le t \le \frac{3\pi}{2} \\ \exp\left(-\frac{(y-r_L-c_y)^2}{2\sigma_L^2}\right) & ; x > c_x. \end{cases} \tag{21}$$

The normalized curvature κ_L is defined by $\kappa_L = \frac{\sigma_L}{r_L}$. In a particular case, according to (21), a corner can be defined by $L(x, y; c_x, c_y, 0, \sigma_L)$, where $r_L = 0$. We synthesized L-junctions with different r_L values.

ACKNOWLEDGMENTS

This work was supported by the Research Fellowships of the Japan Society for the Promotion of Science (JSPS) for Young Scientists (no. 199602316) and the Postdoctoral Fellowships of the JSPS for Foreign Researchers (no. P99078) to Jian Chen. This work was also partly supported by the JSPS Grant-in-Aid for Scientific Research (C) (2) 11680389.

REFERENCES

[1] Y. Sato, S. Nakajima, H. Atsumi, T. Koller, G. Gerig, S. Yoshida, and R. Kikins, "3D Multi-Scale Line Filter for Segmentation and Visualization of Curvilinear Structures in Medical Images," *Medical Image Analysis,* vol. 2, no. 2, pp. 143-168, 1998.

[2] S. Mori and T. Sakakura, "Line Filtering and Its Application to Stroke Segmentation of Handprinted Chinese Characters," *Proc. Int'l Conf. Pattern Recognition,* pp. 366-369, 1984.

[3] L.H. Chen, J.Y. Wang, H.Y. Liao, and K.C. Fan, "A Robust Algorithm for Separation of Chinese Characters from Line Drawings," *Image and Vision Computing,* vol. 14, no. 10, pp. 753-761, 1996.

[4] C.J. Taylor and D.J. Kriegman, "Structure and Motion From Line Segments in Multiple Images," *IEEE Trans. Pattern Analysis and Machine Intelligence,* vol. 17, no. 11, pp. 1,021-1,032, Nov. 1995.

[5] Z.Y. Zhang, "Estimating Motion and Structure from Correspondences of Line Segments between Two Perspective Images," *IEEE Trans. Pattern Analysis and Machine Intelligence,* vol. 17, no. 12, pp. 1,129-1,139, Dec. 1995.

[6] A. Mukherjee, S.K. Parui, B.B. Chaudhuri, R. Krishnan, and K.K. Rao, "Detection of Linear Features in Satellite Imagery Using Robust Estimation," *Proc. 12th IAPR Int'l Conf. Pattern Recognition,* pp. 514-516, 1994.

[7] N. Merlet and J. Zerubia, "New Prospects in Line Detection by Dynamic Programming," *IEEE Trans. Pattern Analysis and Machine Intelligence,* vol. 18, no. 4, pp. 426-431, Apr. 1996.

[8] T.M. Koller, G. Gerig, G. Szekely, and D. Dettwiler, "Multiscale Detection of Curvilinear Structures in 2-D and 3-D Image Data," *Proc. Fifth Int'l Conf. Computer Vision,* pp. 864-869, 1995.

[9] C. Steger, "An Unbiased Detector of Curvilinear Structures," *IEEE Trans. Pattern Analysis and Machine Intelligence,* vol. 20, no. 2, pp. 113-125, Feb. 1998.

[10] J. Chen, Y. Sato, and S. Tamura, "Orientation Space Filtering for Multiple Orientation Line Segmentation," *Proc. IEEE Conf. Computer Vision and Pattern Recognition,* pp. 311-317, 1998.

[11] G.H. Granlund, "In Search of a General Picture Processing Operator," *Computer Vision Graphics, and Image Processing,* vol. 8, pp. 155-173, 1978.

[12] S.W. Zucker, "Early Orientation Selection: Tangent Fields and the Dimensionality of Their Support," *Computer Vision, Graphics, and Image Processing,* vol. 32, pp. 74-103, 1985.

[13] M. Kass and A. Witkin, "Analyzing Oriented Pattern," *Computer Vision, Graphics, and Image Processing,* vol. 37, pp. 362-385, 1987.

[14] P. Perona and J. Malik, "Detecting and Localizing Edges Composed of Steps, Peaks and Roofs," *Proc. Third Int'l Conf. Computer Vision,* pp. 52-57, 1990.

[15] W.T. Freeman and E.H. Adelson, "The Design and Use of Steerable Filters," *IEEE Trans. Pattern Analysis and Machine Intelligence,* vol. 13, no. 9, pp. 891-906, Sept. 1991.

[16] L. Rosenthaler, F. Heitger, O. Kübler, and R. von der Heydt, "Detection of General Edges and Keypoints," *Proc. Second European Conf. Computer Vision,* pp. 78-86, 1992.

[17] M. Michaelis and G. Sommer, "Junction Classification by Multiple Orientation Detection," *Proc. Second European Conf. Computer Vision,* pp. 101-108, 1992.

[18] P. Perona, "Steerable-Scalable Kernels for Edge Detection and Junction Analysis," *Proc. Second European Conf. Computer Vision,* pp. 3-18, 1992.

[19] P. Perona, "Deformable Kernels for Early Vision," *IEEE Trans. Pattern Analysis and Machine Intelligence,* vol. 17, no. 5, pp. 488-499, May 1995.

[20] P. Parent and S.W. Zucker, "Trace Inference, Curvature Consistency, and Curve Detection," *IEEE Trans. Pattern Analysis and Machine Intelligence,* vol. 11, no. 8, pp. 823-839, Aug. 1989.

[21] I.J. Cox, J.M. Rehg, and S. Hingorani, "A Bayesian Multiple Hypothesis Approach to Contour Grouping," *Proc. Second European Conf. Computer Vision,* pp. 72-77, 1992.
[22] N. Katzir, M. Lindenbaum, and M. Porat, "Curve Segmentation under Partial Occlusion," *IEEE Trans. Pattern Analysis and Machine Intelligence,* vol. 16, no. 5, pp. 513-519, May 1994.
[23] P.L. Rosin and G.A.W. West, "Non Parametric Segmentation of Curves into Various Representations," *IEEE Trans. Pattern Analysis and Machine Intelligence,* vol. 17, no. 12, pp. 1,140-1,153, Dec. 1995.
[24] J.H. Elder and S.W. Zucker, "Computing Contour Closure," *Proc. Fourth European Conf. Computer Vision,* vol. II, pp. 397-41,. 1996.
[25] J.M. Chen, J.A. Ventura, and C.H. Wu, "Segmentation of Planar Curves into Circular Arcs and Line Segments," *Image and Vision Computing,* vol. 14, no. 1, pp. 71-83, 1996.
[26] J.G. Daugman, "Uncertainly Relation for Resolution in Space, Spatial Frequency, and Orientation Optimized by Two-Dimensional Visual Cortical filters," *J. Optical Soc. Am. A,* vol. 2, no. 7, pp. 1,160-1,169, 1985.
[27] Y. Sato, J. Chen, R.A. Zoroofi, N. Harada, S. Tamura, and T. Shiga, "Automatic Extraction and Measurement of Leukocyte Motion in Microvessels Using Spatiotemporal Image Analysis," *IEEE Trans. Biomedical Eng.,* vol. 4, no. 4, pp. 225-236, 1997.
[28] Y. Sato, J. Chen, S. Yamamoto, S. Tamura, N. Harada, T. Shiga, S. Harino, and Y. Oshima, "Measuring Microcirculation Using Spatiotemporal Image Analysis," *Proc. First Int'l Conf. Computer Vision, Virtual Reality, and Robotics in Medicine,* pp. 302-308, 1995.
[29] A.P. Witkin, "Scale-Space Filtering," *Proc. Eighth Int'l Joint Conf. Artificial Intelligence,* pp. 1,019-1,022, 1983.
[30] A.L. Yuille and T.A. Poggio, "Scaling Theorems for Zero-Crossings," *IEEE Trans. Pattern Analysis and Machine Intelligence,* vol. 8, no. 1, pp. 15-25, Jan. 1986.
[31] J. Babaud, A.P. Witkin, M. Baudin, and R.O. Duda, "Uniqueness of the Gaussian Kernel for Scale-Space Filtering," *IEEE Trans. Pattern Analysis and Machine Intelligence,* vol. 8, no. 3, pp. 26-33, Mar. 1986.
[32] T. Lindeberg, "Scale-Space for Discrete Signals," *IEEE Trans. Pattern Analysis and Machine Intelligence,* vol. 12, no. 3, pp. 234-254, Mar. 1990.
[33] T. Lindeberg, "Edge Detection and Ridge Detection with Automatic Scale Selection," *Proc. IEEE Conf. Computer Vision and Pattern Recognition,* pp. 465-470, 1996.

Jian Chen received the BS degree in computer science from Fuzhou University, China, in 1984, and the MS and PhD degrees in information and computer sciences from Osaka University, Japan, in 1996 and 1999, respectively. From 1984 to 1992, he worked at Fujian Electronic Computer Company, China, as a software engineer. From 1993 to 1999, he was with the Division of Functional Diagnostic Imaging, Osaka University Graduate School of Medicine, Japan. He was awarded the Research Fellowships of the Japan Society for the Promotion of Science (JSPS) for Young Scientists from May 1996 to March 1999 and the Postdoctoral Fellowships of the JSPS for Foreign Researchers from April 1999 to November 1999. In December 1999, he joined the Department of Radiology, Weill Medical College of Cornell University, where he is currently a member of the academic staff working on medical image analysis. His research interests include computer vision and its applications to medical image analysis. Dr. Chen is a member of the IEEE.

Yoshinobu Sato received the BS, MS, and PhD degrees in information and computer sciences from Osaka University, Japan, in 1982, 1984, 1988, respectively. From 1988 to 1992, he was a research engineer at NTT Human Interface Laboratories. In 1992, he joined the Division of Functional Diagnostic Imaging of Osaka University Medical School as a faculty staff member. From 1996 to 1997, he was a research fellow at the Surgical Planning Laboratory, Harvard Medical School and Brigham and Women's Hospital. He is currently an associate professor at the Osaka University Medical School. He leads the research group on 3D image analysis and surgical navigation systems of the Division of Functional Diagnostic Imaging at Osaka University Medical School. Dr. Sato is a member of the IEEE.

Shinichi Tamura received the BS, MS, and PhD degrees in electrical engineering from Osaka University, Japan, in 1966, 1968, and 1971, respectively. He is currently a professor of the medical school, and Graduate School of Engineering Science, at Osaka University. He is the author/coauthor of more than 180 papers in scientific journals and has received several paper awards from journals/societies, including *Pattern Recognition* and *Investigative Radiology*. His current research activities include work in the field of image processing and its medical applications. Dr. Tamura is a member of the IEEE, the International Society for Computer Aided Surgery, the Institute of Electronics, Information and Communication Engineers of Japan, the Information Processing Society of Japan, the Japanese Society of Medical Imaging Technology, and the Japan Radiological Society. Currently, he is an associate editor of *Pattern Recognition*, and a vice-editor-in-chief of *Medical Imaging Technology*.